Czech Technical University in Prague
Faculty of Nuclear Sciences and Physical Engineering

Department of Physics

Silicon Drift Detectors

Review Work

Jiří Král

Supervisor: RNDr. Vojtěch Petráček

Table of contents

1. Introduction

A new type of two dimensional silicon detectors was introduced in 1983, taking advantage of a newly described electron transportation scheme in fully depleted semiconductor. A semiconductor wafer is fully depleted (freed of majority charge carriers) to allow creation of uniform drift field. A passing particle generates electron-hole pairs, the present drift field makes electrons to drift in a given direction towards a readout region that is situated at one border of the wafer.

This approach allows to reduce amount of needed readout electronics in comparison with strip and pixel detectors making is simpler to manufacture and implement. Very good performance in high multiplicity environment and good spatial resolution, which is under 30 μm, makes the silicon drift detector ideal for tracking in high energy physics application. The downside of the approach is a rather long drift time of electrons which makes it difficult to use the SDD in environments with very high event rate.

2. Principles of Silicon Drift Detectors

2.1 Semiconductor depletion

To achieve a electric field form suitable for electron transport within a detector, a n-type silicon wafer must be first freed of free majority charge carriers (i.e. electrons). Fig. 2.1a shows a n-type silicon wafer with p+n rectifying junction contacts on both sides. Applying a similar reverse bias voltage on both junction contacts leads to creation of a depleted region close to the junction contacts, as seen on Fig 2.1b. The middle part of the wafer acts as a conductor leading electrons away from the wafer. The thickness of undepleted middle region decreases with increasing bias voltage applied on junction connectors, until the limiting case of whole depletion, when the middle conductive region has fully diminished. Fig. 2.1c. Positive charge of ionized donors is compensated with the same magnitude of negative charge present on p+n junctions on sides of the wafer.

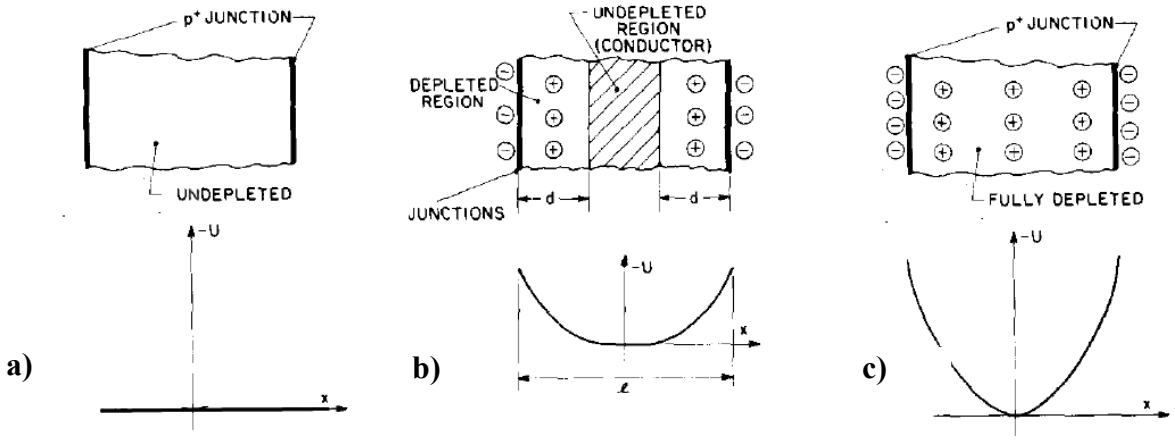

Fig 2.1 Depletion stages. a) Junctions on opposing sides of the wafer. b) Partially depleted wafer, when the bias voltage was applied. c) Fully depleted. The central conductive channel has disappeared.

2.2 The drift field

U shaped field applied perpendicularly to the wafer pane does not allow yet for transport of electrons generated by passage of a fast ionizing particle, which is necessary for detector functionality and for stability of the depleted state. The parabolic potential is constant over the third (z) coordinate, making it a two-dimensional problem. Since a fully depleted detector is considered, the negative potential must comply to the Poisson's equation:

$$\frac{\partial^2(-\Phi)}{\partial x^2}+\frac{\partial^2(-\Phi)}{\partial y^2}=\frac{N_D q}{\varepsilon_0 \varepsilon_r} \quad , \tag{1}$$

where N_D is the density of ionized donors in silicon bulk; q electric charge; ε_r relative dielectric constant; ε_0 is the permeability.

The negative potential function as shown on Fig. 2.2 is the result of superposition of the parabolic shaped potential along x axis and a linear drift potential created along the y axes, which inclines the resulting function, so the generated electrons are slided away from the point of their origin towards the readout region. The ideal negative potential is described as:

$$-\Phi_i=\frac{N_D q}{2\varepsilon_0 \varepsilon_r}(x-x_0)^2+E_D y \quad , \tag{2}$$

x_0 is a coordinate of the potential minimum and E_D is the drift field.

Fig 2.3 shows an example of realization of a drift chamber. The surface is covered by a strip array of p+n junctions along z axis. Potential applied on to the two opposing (top and bottom) strips provides the depletion. Cascade of potential along y axes (in between two neighboring strips) provides the drift field. Electrons generated by passage of a fast ionizing particle are sliding in the potential valley in the uniform field towards the end of the wafer (by y axes). While being pulled to the center (by z-axis) of the wafer, their movement is screened by p+n junction stripes acting as electrodes. The drift time of electrons is proportional in uniform field to the distance of reaction point of the particle. Anode placed down the stream registers electrons coming close to it. Hence the delay between passage of a particle and the signal from the anode is dependent on drift time of the electron pack within the wafer.

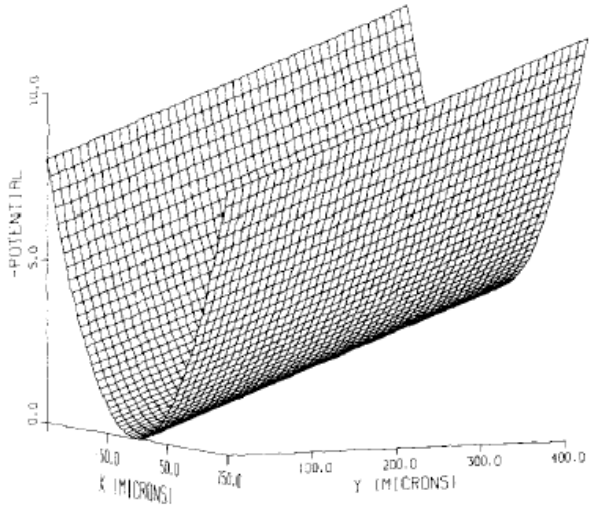

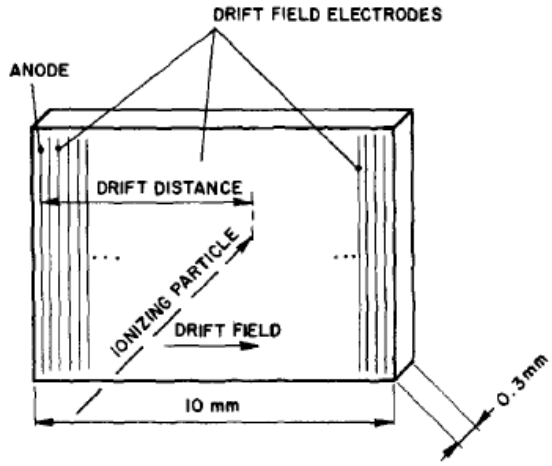

Fig 2.2 The ideal negative potential of fully depleted semiconductor detector, when a additional linear lateral field is applied.

Fig 2.3 Silicon drift chamber. The surface is covered by a strip array of p+n junctions which provide the depletion and the lateral drift field. (Only junctions at the extremes of the chamber are shown.)

2.3 Additional electric field formation

In theory, the best location for readout anode would be right in the middle of wafer side, where the potential on Fig 2.2 leads the drifting pack of electrons. Such a setup is not easy to be achieved because of difficulties during fabrication process. Therefore the readout anode is likely to be placed along the p+n junctions on one side of the wafer (Fig 2.5). This setup requires the drift field to be modified, so that electron paths curve to the readout anode as the pack approaches close to the end of the wafer. (Fig 2.4)

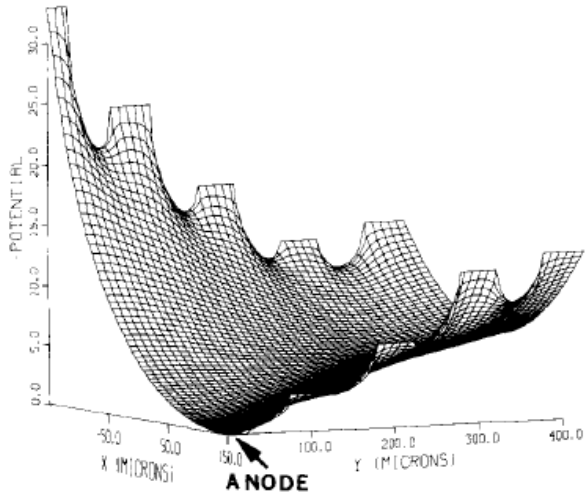

Fig 2.4 The negative potential within the drift chamber close to the readout anode. The p+n junctions opposite to the readout anode are biased to higher negative potential, while the junctions on the anode side are biased less negatively.

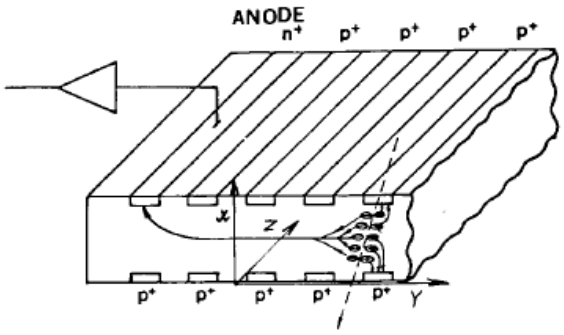

Fig 2.5 Silicon drift chamber principle. Electrons created by ionizing particle are transported for a long distance through the wafer to the detector surface onto a small capacitance anode.

3. Electron dynamics

The shape of traveling electron packet is not constant in time. External electric field, mutual electrostatic repulsion in between generated electrons and electron diffusion properties of particles act to change the initial electron distribution.

Some simplification should be made in order to study theoretical behavior. Effect of holes is neglected, supposing that they are collected immediately by the p+ electrodes. Any processes that occur shortly during electron/hole generation are neglected. So that analysis begins with a pack of electrons only. Neglecting mutual electrostatic repulsion in between generated electrons, in the first case studied, allows to study electric field and diffusion effect. The repulsion effects are taken into account in section 3.2.

3.1 Diffusive dynamics of electrons

Neglecting mutual repulsion effects of generated electrons makes the dynamics to depend on diffusive precesses of particles and the external electric fields.

The external electric field, as it is generated by fixed charge on p+ electrodes, has a component E_x perpendicular to the detector plane, component E_y that is in parallel to the plane and in parallel with electron packet movement, component E_z is than in parallel to the plane and perpendicular to electron packet movement. E_z is equal to zero, E_y represents the slide towards one end of a wafer and can be taken as a constant in a first approximation. E_x , which is generate by fixed electrostatic depletion charge, can be written as:

(3) $$E_x = \frac{N_D q}{\varepsilon} x = Kx$$

Which corresponds to potential on Fig 2.2.

The motion of electrons can be decomposed into three directions which are along axes of the wafer. Movement in z direction is free of any confining forces and is therefore a free diffusion. The longitudinal electron density along this axes has a form of a gaussian:

(4) $$n(z,t) = \frac{1}{2\sqrt{\pi\, Dt}} \exp\left(\frac{-y^2}{4\mathrm{Dt}}\right) \quad ,$$

where D is a diffusion constant.

Movement in y direction is a free diffusion superposed on a uniform shift towards the end of a wafer.

(5) $$n(y,t) = \frac{1}{2\sqrt{\pi\, Dt}} \exp\left(\frac{-(y-\mu\, E_x t)^2}{4\mathrm{Dt}}\right)$$

Along the x axis, continuity equation taking into account diffusion and drift currents, gives:

(6) $$\frac{\partial^2 n}{\partial x^2} - \frac{1}{D}\frac{\partial n}{\partial t} + \frac{K}{V_T}\left(n + x\frac{\partial n}{\partial x}\right) = 0 \quad ,$$

where V_T is the thermal voltage kT/q, $n = n(x,t)$. The solution for n(x,t) s given by series expansion in terms of Hermite polynomials:

(7) $$n(x,t) = \sum_0^\infty A_m \exp\left(\frac{-Kx^2}{2\mathrm{V}_T}\right) H_m\left(x\sqrt{\frac{K}{2\mathrm{V}_T}}\right) \exp\left(\frac{-mKDt}{V_T}\right)$$

The first term (m=0) does not decay with time and represents the asymptotic distribution, when diffusion is compensated by focusing effects of external field.

(8) $$n(x,\infty)=A_0\exp\left(\frac{-Kx^2}{2V_T}\right)$$

Two examples of possible n(x,t) evolution are shown on fig 3.1 and fig 3.2. The distribution reaches the same distribution described by (8) in both cases.

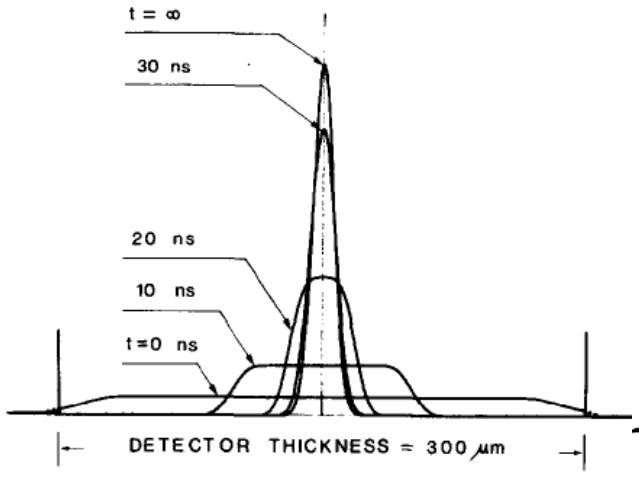

Fig 3.1 Longitudinal distribution of electrons generated by interaction of a minimum ionizing particle interacting perpendicularly to the detector plane. Time evolution.

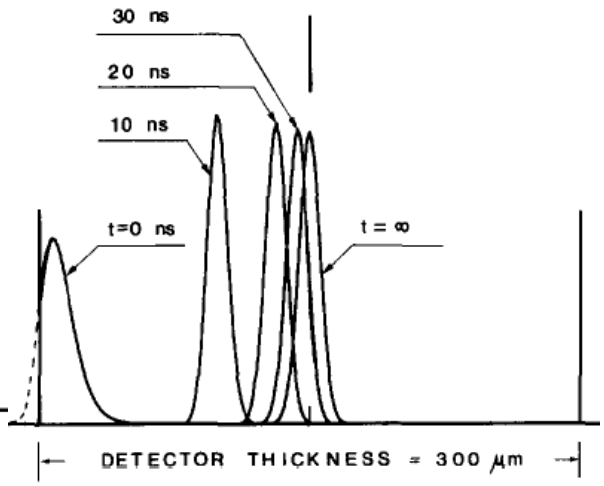

Fig 3.2 Initial charge generation close to surface of detector wafer. (by light pulse or low energy X-ray) Time evolution.

The volume density of electrons can be obtained as a product of all three longitudinal densities. The shape of traveling electron packet is a disk with a more or less constant thickness of about 15μm in x direction. It increases its diameter in y and z directions as a result of free diffusion.

3.2 Flat disk geometry

This model considers two-dimensional motion of a packet of N charges in a cylindrical symmetry shown on fig 3.3. It also considers effects of mutual repulsion of generated electrons. The continuity equation has the form of:

(9) $$\frac{\partial^2 Q}{\partial x^2}-\frac{1}{r}\frac{\partial Q}{\partial r}-\frac{1}{D}\frac{\partial Q}{\partial t}-\frac{E}{V_T}\frac{\partial Q}{\partial r}=0 \quad ,$$

where *Q(r)* is:

(10) $$Q(r,t)=\int_0^r n(r,t)\,2\pi r\,dr \quad ,$$

where *n(r;t)* is electron density per unit of area.

E(r) is a radial field which depends on all charges within the disk and within its electrical images (as shown on fig 3.3).

(11) $$E = \frac{-\partial V}{\partial r} \quad ,$$

where:

(12) $$V(r) = \sum_{-\infty}^{\infty} \frac{q}{\pi e} (-1)^m \int_0^{\infty} n(\tilde{r})\, \tilde{r}\, \frac{F\left(\frac{\pi}{2\alpha}\right)}{\sqrt{x_m^2 + (r+\tilde{r})^2}}\, d\tilde{r} \quad ,$$

where $x_m = md$, $F(\pi/2\alpha)$ is the elliptical integral of first kind and:

(13) $$\alpha = arctg\left(\frac{2\sqrt{(r\tilde{r})}}{\sqrt{(r+\tilde{r})^2 + x^2}}\right) \quad ,$$

The electron density *n(r,t)* can be obtained from eq. 10. It is useful to project *n(r,t)* to *n(y,t)*, since *n(y,t)* can be measured as a signal coming from readout anode over time.

(14) $$n^*(y,t) = \int_{-\infty}^{\infty} n(r,t)\, dz = 2 \int_{r=|y|}^{\infty} \frac{n(r)}{\sqrt{1 - (y/r)^2}}\, dr \quad .$$

Fig 3.4 shows projected $n^*(y,t)$ for different N of electrons in different times. Fig 3.5 shows the rms broadening over time.

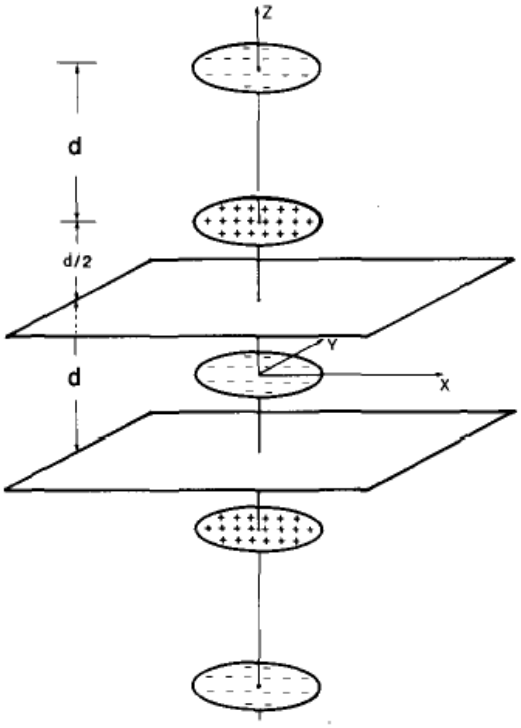

Fig 3.3 Schematic view of the detector surfaces with spacing d, of the confined electron disk at the center of the wafer and of its electrical images.

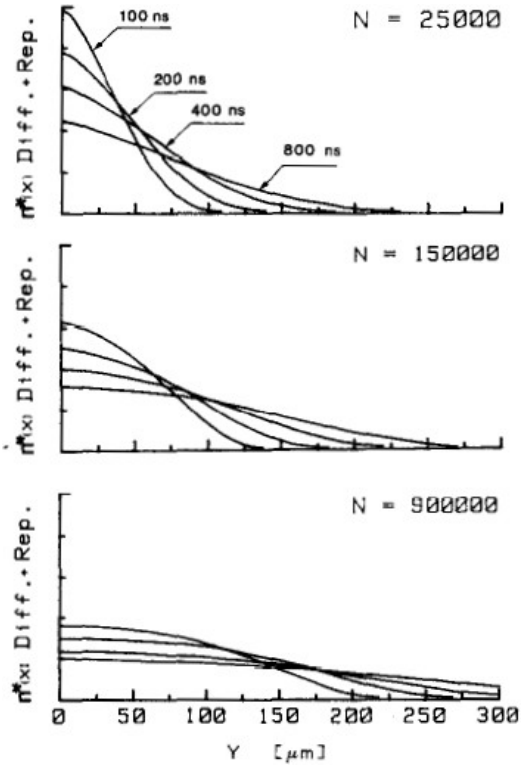

Fig 3.4 Spatial distribution of the disk clouds projected onto drift direction, as due to diffusion plus repulstion.

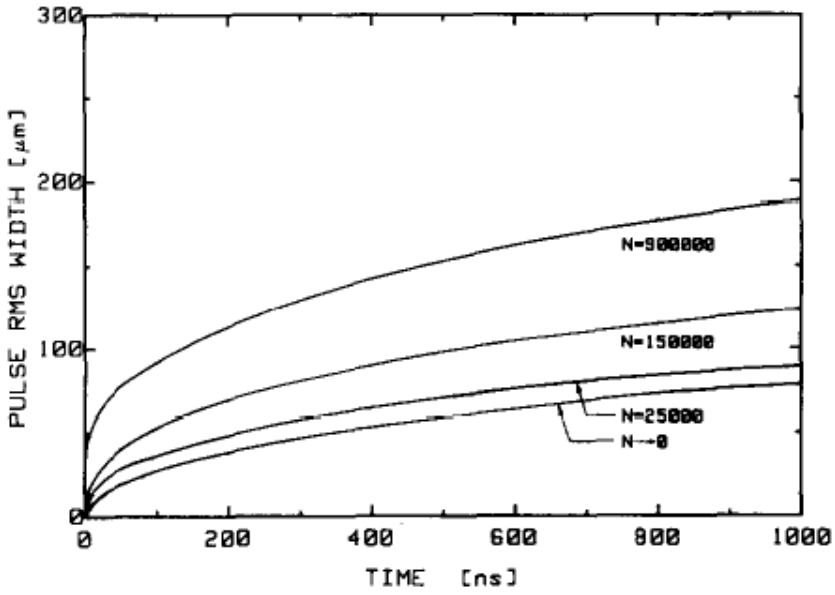

Fig 3.5 Rms spatial pulse width of the projected cloud on the drift direction versus time elapsed for different N of electrons.

4. Signal processing

In an ideal case, not considering any sources of fluctuation, the form of signal induced at the anode would be as seen on fig 4.1. The electron speed in y direction is constant in potential on Fig 2.2, so the electrons generated by passing (perpendicularly) ionizing particle arrive at the same time to the readout anode. It would then be easy to determine the impact distance of the passing particle using the drift speed and time. The time can be obtained by using a parallel triggering detector. Only the hight of the peak would variate depending on the ionization loss of the particle.

4.1 Fluctuation sources

In the real experiment, random fluctuations interfere with an ideal signal. The sources of those interferences are: detector leakage current, series amplifier noise, electron diffusion and mutual repulsion. The detector leakage current is generated by thermal generation of electron-hole pairs. The series amplifier noise is given by power spectrum density of the amplifier. The last source of fluctuation was described in chapter 2. Fig 4.2 shows examples of a real pulses for different particle crossing distance.

Linear filters are being placed to decrease the time variance when the signal crosses a defined threshold. The signal level discrimination is placed at the filter output. The detail derivation of such a filter is described in [2]. Use of the filter limits the time window in which the signal crosses the threshold and thus increases the longitudinal resolution of the detector.

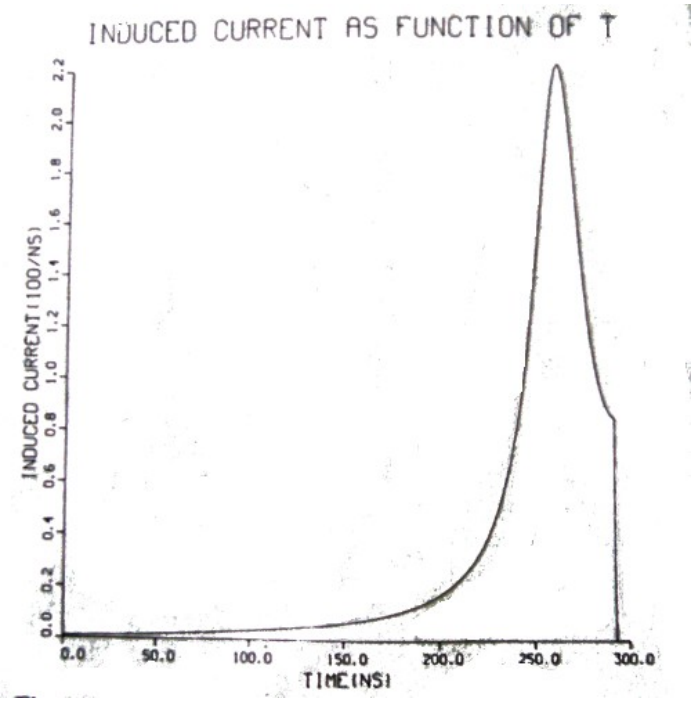

Fig 4.1 A ideal signal shape.

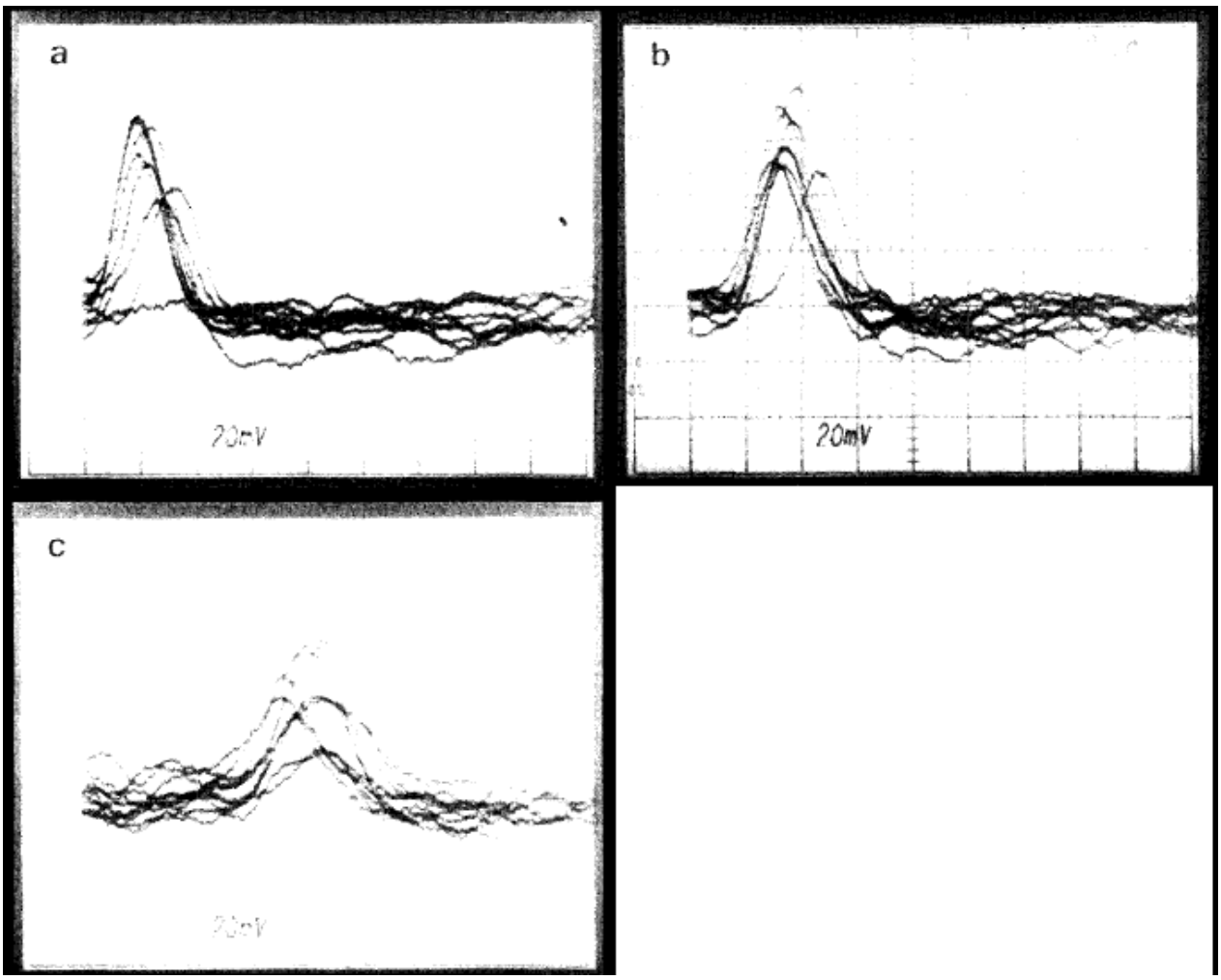

Fig 4.2 Gaussian shaped signals of a drift chamber; a) β test beam directed on top of the readout anode; b) test beam shifted 0.5 mm from the anode; c) test beam at distance 1.5 mm from the anode

4.2 Resolution

The contribution of amplifier noise to the fluctuation increases with increasing drift velocity, the other two contributions decrease. Therefore it is possible to compute a optimal drift velocity. Example [2] states 1-2 μm / ns for 300 μm of wafer thickness with resolution of 2 – 5 μm.

5. Double particle resolution

Signal coming from two particles impacting close to each other sums up. Recognition of the two Gaussian pulses is necessary to determine particle impact points. Example signal functions are shown on fig. 5.1.

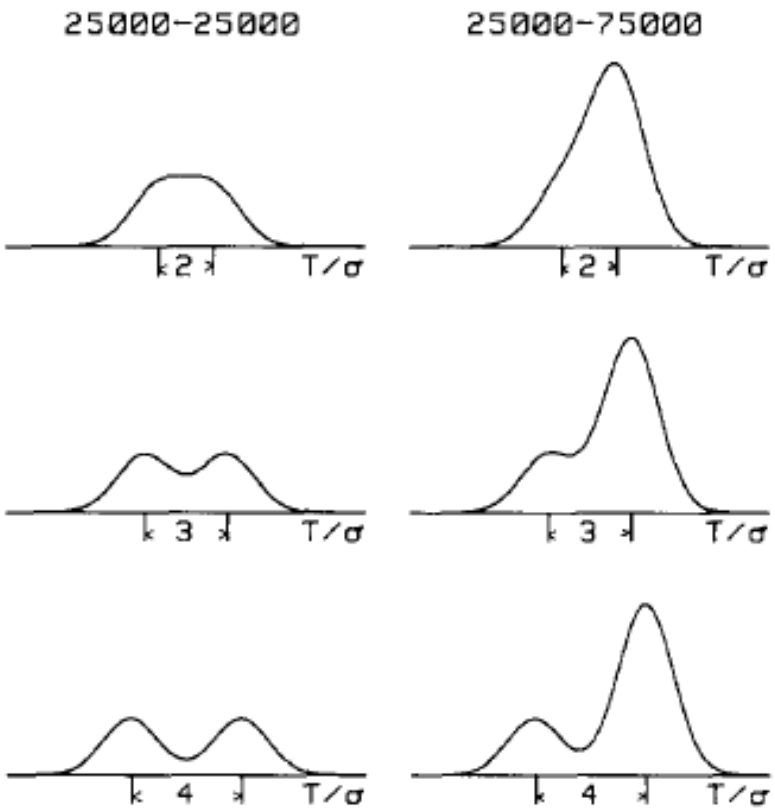

Fig 5.1 Two superimposed Gaussians of simmilar (25000) or different (25000, 75000) electron counts in different spacings normalized to rms.

To solve the problem, one must find centroids of the two Gaussians and their variances to get the position and resolution along the drift coordinate. Determination of amplitudes gives position in the perpendicular axis.

In addition to summing two Gaussians, different additive fluctuations modify the signal, such as leakage current, shot noise or amplifier noise. Also a Poisson noise shall be considered. Paper [6] provides a detail explanation of such effects.

6. Drift path deviation

Accuracy of the drift detectors is very sensitive to the drift field uniformity. Two coordinates of a impact point of a particle are computed using the time electron packet spends moving towards readout anode array and the position of the packet centroid as it hits the anodes. If a non-uniformity is introduced in the drift field, the packet's path may be modified or it's drift speed can get slower or faster resulting in uncertainty if coordinate determination. En example of such a path is shown on fig. 6.1.

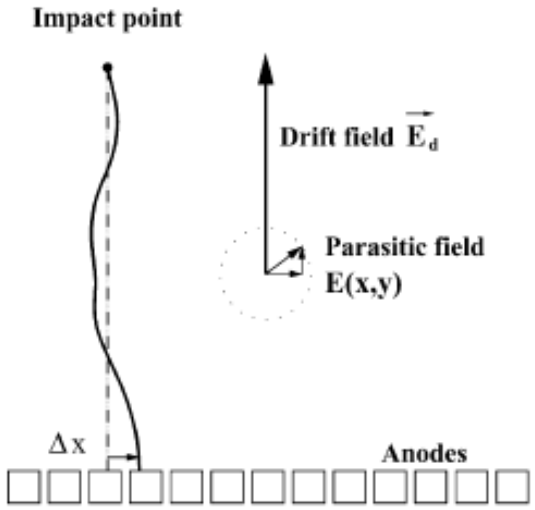

Fig 6.1 Electron packet path in a wafer in presence of parasitic fields.

Drift field non-uniformity is caused by superimposed parasitic fields. The most important source of such parasitic fields is inhomogeneity of dopant distribution in the wafer, which leads to systematic deviation in determination of impact point coordinates. A measurement was done for a wafer which was planned to be used in ALICE experiment. Two microstrip detectors placed above and below the measured wafer were used to determine particle impact point with accuracy of 5 μm. A systematic deviation in anode axis was measured fig 6.2.

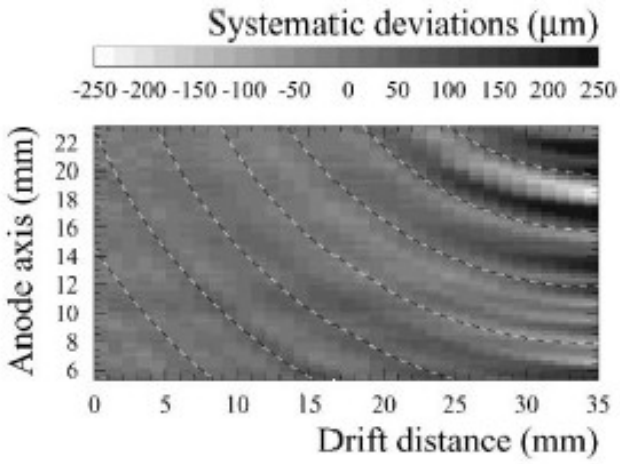

Fig 6.2 Systematic deviation of the electron packet centroid in anode axis.

Circular structure visible is attributed to the fabrication process, where the dopant concentration fluctuations are radially dependent. Spatial resolution required for the wafers is 30 μm. Since the largest deviation measured was 300 μm, drift path deviation effects must be accounted for. Anodic resolution as a function of drift distance is shown on fig. 6.3. The deviation may be partially eliminated with increasing the intensity of the drift field (fig 6.4), which at the other hand increases fluctuation coming from the amplifier noise.

Correction maps must be created for each production wafer. Scanning the wafer with infrared laser was used for SDD wafers for ALICE experiment.

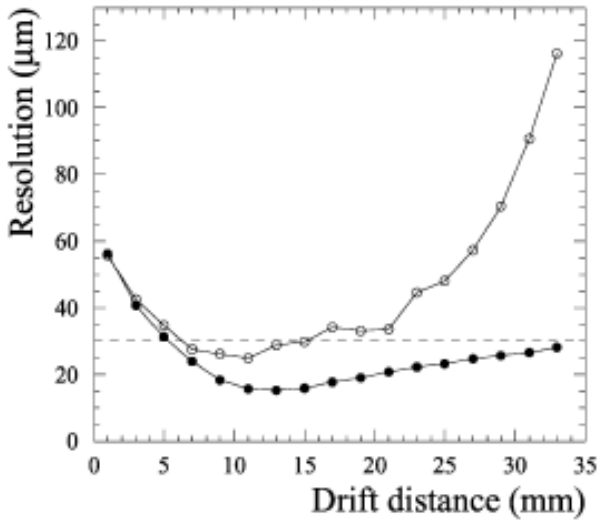

Fig 6.3 Anodic resolution of a drift detector with (full) and without (void) systematic error correction. The resolution is defined as a rms of residuum of measurements of SDD and microstrips.

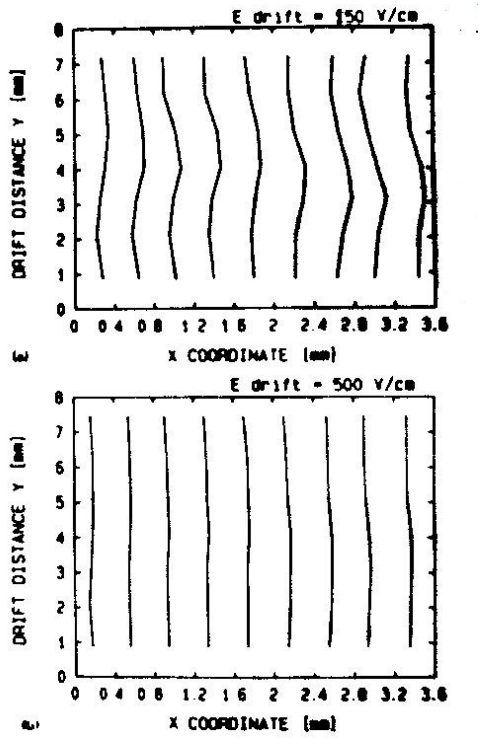

Fig 6.4 Drift paths in different field intensities.

7. Electron Injection

Drift velocity of electrons in silicon is dependent on the temperature. The dependence is approximately 1%/K.

(15) $\mu \approx T^{-2.4}$.

The necessity to monitor the drift velocity arises because of the factor of dependence. The monitoring can be done by artificially creating a cloud of electrons at a given distance and time. Using a light pulse is a good method for lab tests, but hard to achieve in experiments. A new device to inject electrons was introduced.

7.1 Injectors

Injector is a MOS diode (metal on silicon dioxide), placed in between the p^+ anodes (fig. 7.1).

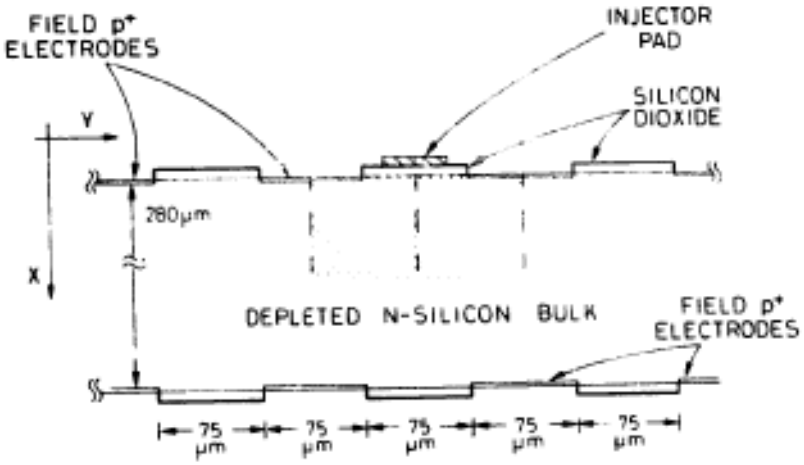

Fig 7.1 Cross section of a SDC in the region of the injector.

It's function is not to directly inject electrons, but to change a shape of the electric field when a pulse arrives. Due to the bias applied to the p^+ electrodes, charge accumulated in the dioxide and the space charge of the depleted detector, there is a small saddle point close to the injector plate (fig 7.2). The boundaries of the saddle point are created by presence of bias (in y direction). Boundaries in x direction are created by superposing all three fields, which creates a small rise in potential prior to descent to the form of parabolic potential which is expected in depleted wafer.

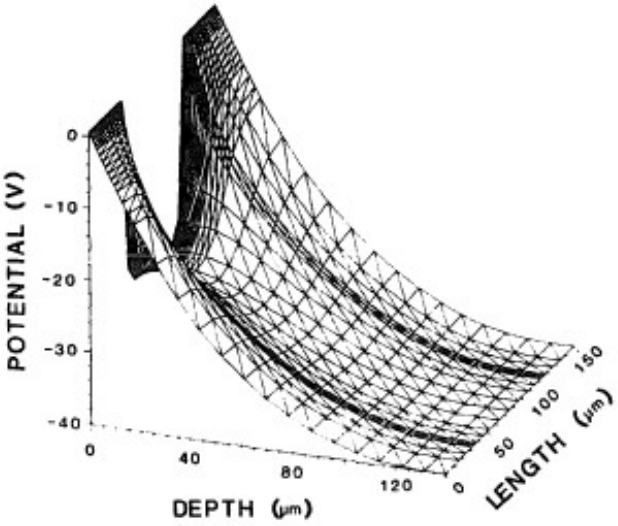

Fig 7.2 potential in the region of the injector.

The existence of the saddle works as a trap for electrons, which accumulate there due to the surface and bulk generation. The amount of charge accumulated is dependent on equilibrium in between generation and amount of charge that leaks over the potential barrier of the saddle.

Short negative pulse presented to the injector pad lowers the potential barrier, so a fraction of electrons is free to move inside the wafer. Since there are many electrons to supply the saddle in z direction (parallel to p^+ electrodes), the pulse can repeat very fast. Fig 7.3 shows the amplitude of charge inserted as a function of amplitude of injector voltage pulse. Saturation visible for amplitudes over 2V is due to near complete depletion of the saddle.

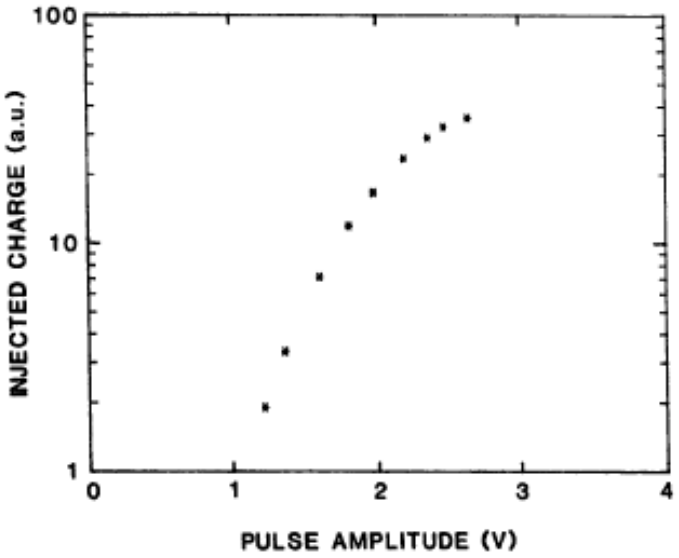

Fig 7.3 charge amplitude dependence on the voltage pulse applied to the injector

8. Drift Detectors in Experiments

Multiple generations of silicon drift detectors have been used in both running and discontinued experiments, used mainly for tracking purposes.

8.1 CERES/NA45

The CERES experiment was based on CERN's LEP. Was build to observer electron-positron pairs induced by relativistic nuclear collisions. The experiment is of a static target design optimized for measurements of electrons in range of 50MeV/c^2 to 1.5GeV/c^2. CERES operation started in 1992 and lasted until year 2000. The experiment went through two upgrades during it's operation. Two Silicon Drift Chambers were added during the first upgrade in 1994/5. A radial Time Projection Chamber was added during the second upgrade in 1998. Fig.7.1 shows the experiment setup.

The main detectors are the Ring Imaging Cherenkov detectors. SDDs are used for tracking and vertex reconstruction. Two AZTEC SDD detectors are placed in telescope located approximately 10cm far from target area allowing to register particles in 8° to 15° exit angle.

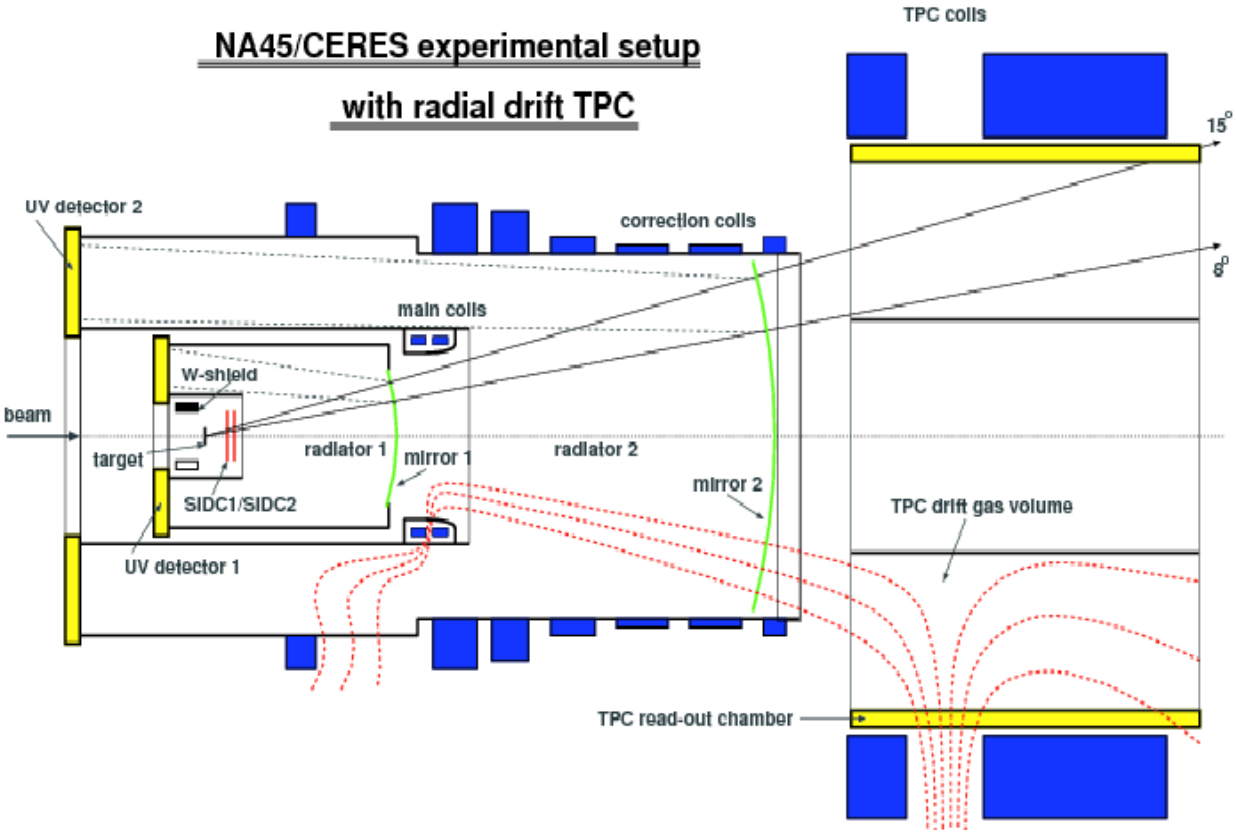

Fig 8.1 CERES experiment 1998

AZTEC is a 55 cm^2 cylindrical detector. Cylindrical geometry is approximated by 360 readout anodes making 360 sided polygon. Special design of interlaced anodes (anodes are made of interconnected stripes) improves approximation of ideal circles. Injector pads are implemented in three levels. Fig 8.2.

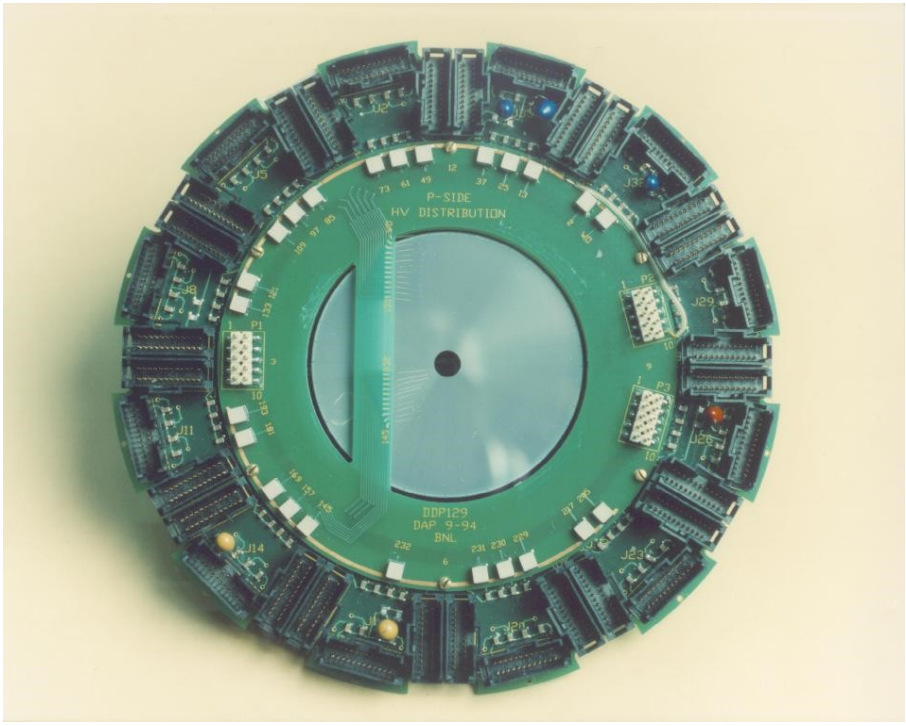

Fig 8.2 AZTEC SDD detector

8.2 STAR

The STAR is a running experiment at RHIC at Brookhaven National Laboratory. Was build primarily for study of Quark Gluon Plasma. It's main detector is the Time Projection Chamber. Silicon Vertex Tracker is build solely from SDDs composed into three barrels.

New generation of SDDs and new geometry added more functionality to the SVT in comparison with the CERES experiment. SDDs are organized in ladders (fig 8.3) into 3 complete barrels surrounding the interaction point. Energy loss measurements are possible in between the barrels to ease the particle identification. Secondary vertex reconstruction searches for short lived particles (mainly strange and multi-strange baryons). SVT also enhances accuracy of primary vertex reconstruction and double track separation.

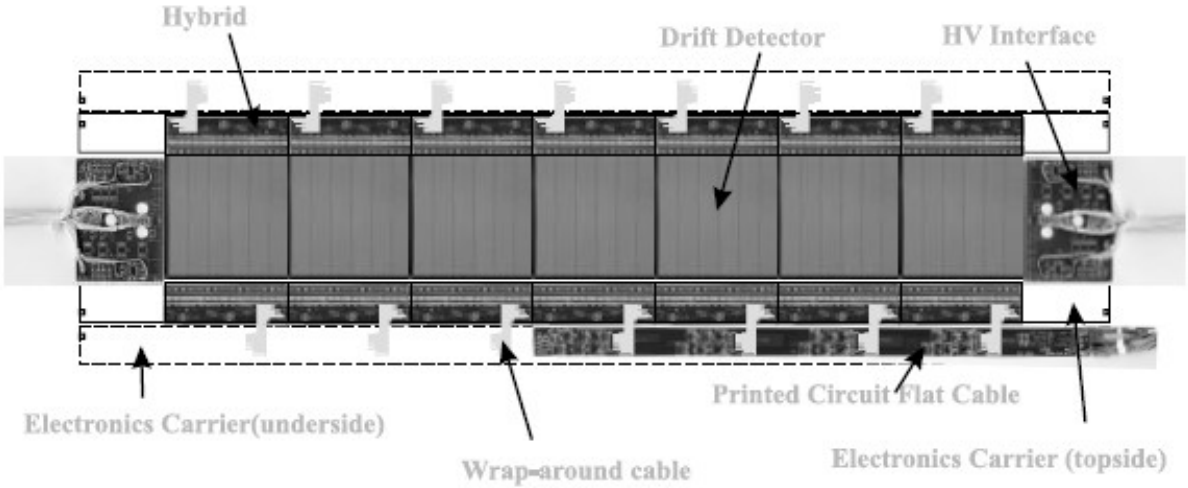

Fig 8.3 Layer 3 SVT ladder with 7 SDD wafers.

The wafer resolution is in order of 20 µm. Some wafer characteristics are shown on fig 8.4.

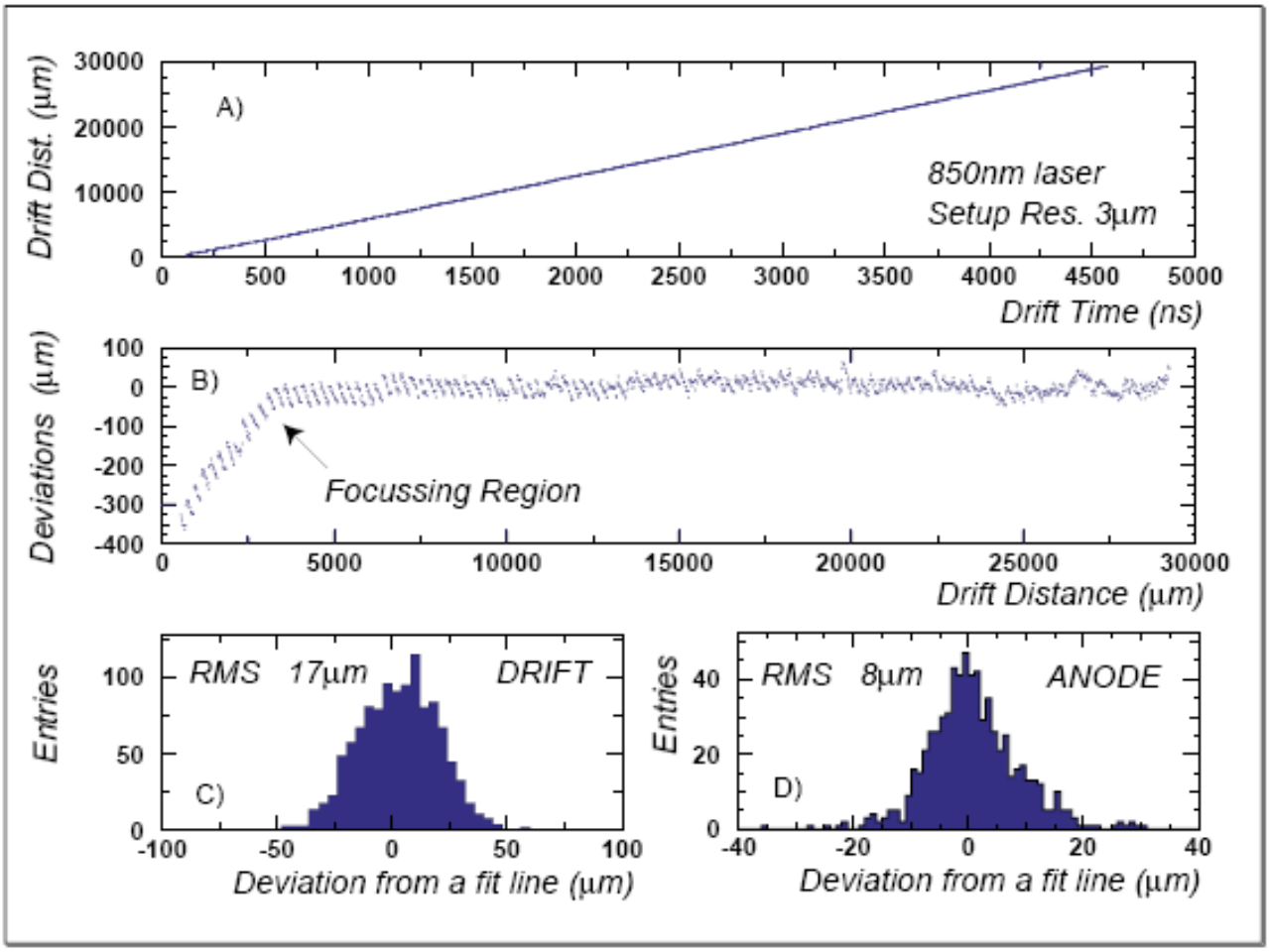

Fig 8.4 A) Laser measurement of drift time vs. drift distance. B) Difference between data points and straight line fit. C) Histogram of the difference B. D) Histogram of difference of actual and reconstructed position of laser injection in anode direction.

Fig 8.5 SVT in middle of construction

9. Drift Detectors in ALICE

A Large Ion Collider Experiment is currently in last stages of construction at CERN's new LHC accelerator. It's main purpose is to study Quark Gluon Plasma generated by Pt-Pt collisions @ 5.5TeV or p-p @ 15 TeV. ALICE is 4Π detector composed of different functionality layers. Innermost are trackers followed by particle identification and calorimeters and muon detectors. Main tracking detector is the Time Projection Chamber, which is supported by silicon detectors based Inner Tracking System used in the innermost layers, where the particle density goes up to 90 per cm^2. Multiple generations of silicon drift detectors have been used in both running and discontinued experiments, used mainly for tracking purposes.

9.1 Inner Tracking System

The ITS is composed of six layers of silicon detectors. High particle densities close to the beam pipe require usage of two-dimensional detectors. First two layers are composed of pixel detectors followed by two layers of drift and two layers of micro strip detectors (fig 9.1).

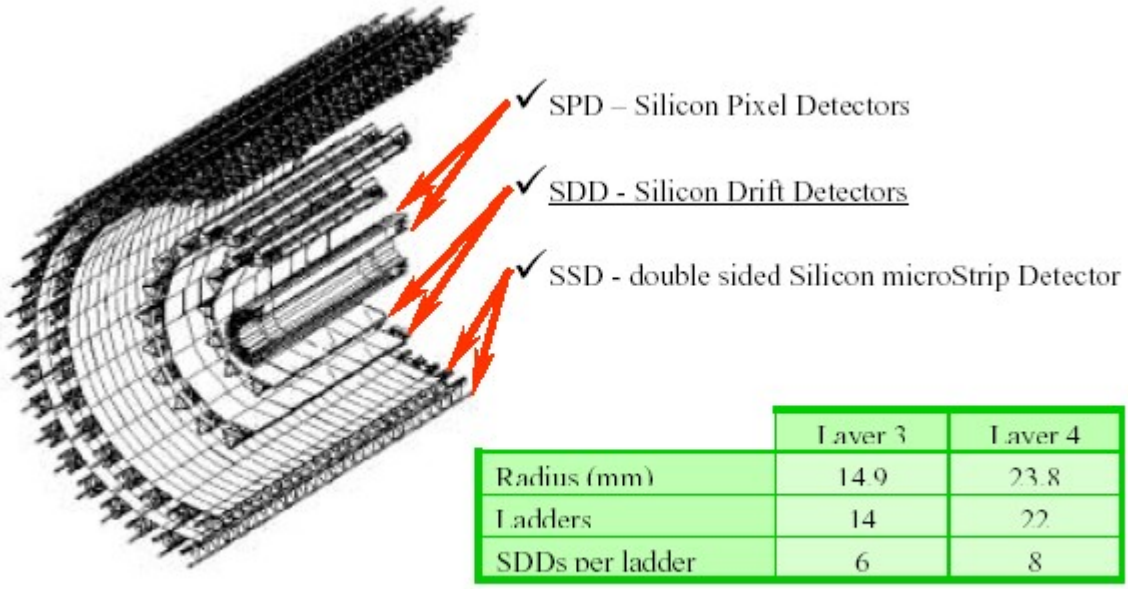

	Layer 3	Layer 4
Radius (mm)	14.9	23.8
Ladders	14	22
SDDs per ladder	6	8

Figure 1 - Silicon Drift Detector layers

Fig 9.1 ALICE ITS

Main purpose of ITS is secondary vertex reconstruction of hyperon and charm decays, particle identification and low momentum particle tracking. ITS is the only detector which can track particles under 100MeV/c. Possibility of D meson detection is also foreseen.

9.2 The Drift Layer

Each of the two SDD barrels is composed of ladders (fig 9.2) of detectors (table on fig 9.1), summing up to 260 detector wafers in place. Ladder is a carbon fiber plastic structure which supports all cabling, front-end electronics and detector wafers. Spatial resolution is approximately 30μm and double-track resolution in order of O(600). Detector wafers (fig 9.3) are 300μm thick with active area of 7.02 x 7.53 cm.

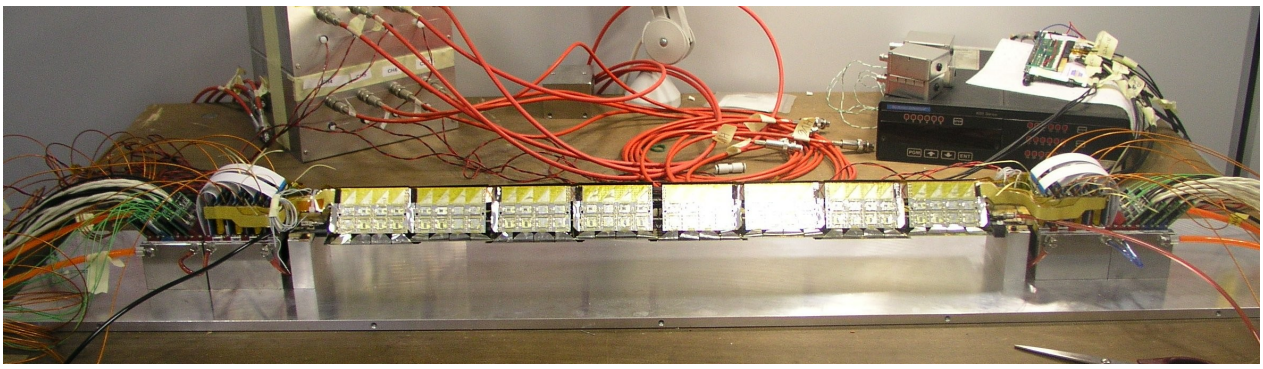

Fig 9.2 Layer 4 ladder with 8 detector wafers at the bottom, DAQ chips at the top and front-end electronics by the sides.

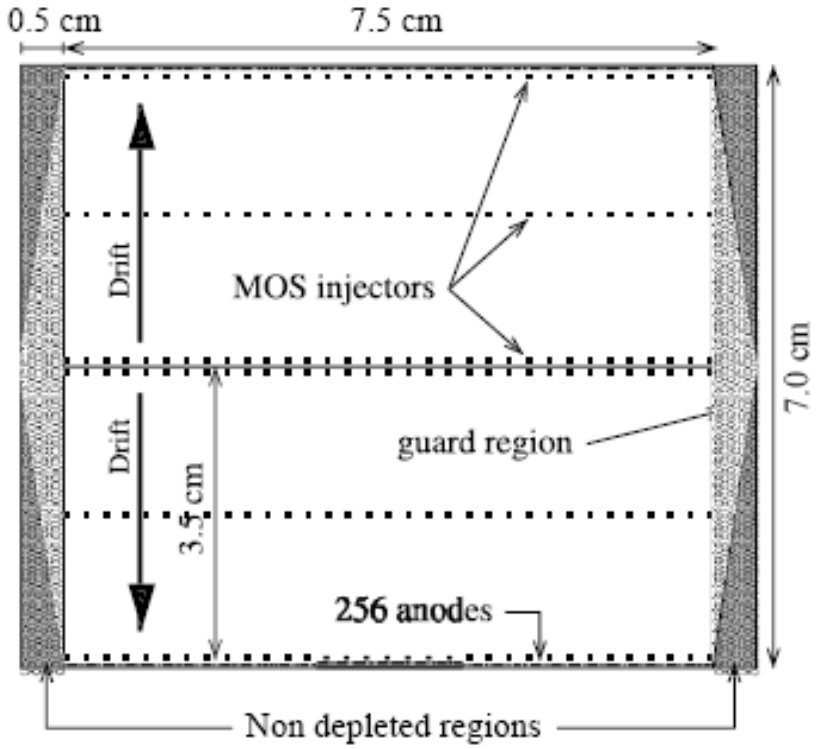

Fig 9.3 ALICE SDD wafer

The wafer is divided into two regions, each is terminated with array of readout 256 anodes. Electron mobility is monitored by 3 rows of 33 MOS injectors. The orientation of anodes (and the vector of drift velocity) is so, that the Lotenz force effects are compensated by the focusing field in z coordinate.

10. Conclusion

Silicon Drift Detectors have gone through intense development since it's proposal in early 80s. Behavior of electron packet inside wafer has been described and many problems arising from real-world behavior have been resolved. Resolution of SDDs is in order of few tens of micrometers, suitable enough form high energy physic. SDD's high multiplicity registration ability makes them ideal to be used in tracking systems. Stable wafer production and techniques are available and SDDs are being used in large scale experiments.

11. Literature

[1] E. Gatti and P. Rehak, *Nucl. Instr. and Meth. A*225, (1984) 608

[2] E. Gatti and P. Rehak, *Nucl. Instr. and Meth. A*226, (1984) 129

[3] P. Rehak and E. Gatti, *Nucl. Instr. and Meth. A*235, (1985) 224

[4] P. Rehak and J. Walton, *Nucl. Instr. and Meth. A*248, (1986) 367

[5] E. Gatti and P. Rehak, *Nucl. Instr. and Meth. A*226, (1987) 393

[6] E. Gatti and P. Rehak, *Nucl. Instr. and Meth. A*274, (1989) 469

[7] A. Vacchi, *Nucl. Instr. and Meth. A306*, (1991) 187

[8] A. Vacchi and P. Rehak, J. Appl. Phys. *71 (7)*, (1992) 3593

[9] W. Chen, H. Kraner, Z.Li and P. Rehak, *Nucl. Instr. and Meth. A326*, (1993) 273

[10] E. Gatti and P. Rehak, *Nucl. Instr. and Meth. A377*, (1996) 367

[11] E. Gatti and P. Rehak, *Nucl. Instr. and Meth. A399*, (1997) 227

[12] D. Nouais, et al., *Nucl. Instr. and Meth. A461*, (2001) 222

[13] D. Nouais, et al., *Nucl. Instr. and Meth. A477*, (2002) 99

[14] D. Nouais, et al., *Nucl. Instr. and Meth. A501*, (2003) 119

[15] ALICE Technical Design Report